CRYSTAL GROWTH & DESIGN

pubs.acs.org/crystal

Article

Influence of Synthesis Time on the Morphology and Properties of CeO_2 Nanoparticles: An Experimental–Theoretical Study

Regiane Cristina de Oliveira,* Rafael Aparecido Ciola Amoresi, Naiara Letícia Marana, Maria Aparecida Zaghete, Miguel Ponce, Adenilson José Chiquito, Julio Ricardo Sambrano, Elson Longo, and Alexandre Zirpoli Simões

Cite This: *Cryst. Growth Des.* 2020, 20, 5031−5042

Read Online

ACCESS | Metrics & More | Article Recommendations | Supporting Information

ABSTRACT: Here we combined experimental and theoretical results to correlate the morphological, optical, and electronic properties of cerium oxide (CeO_2) prepared by a microwave-assisted hydrothermal method with varying synthesis times. X-ray diffraction confirmed a cubic structure without deleterious phases. Density functional theory simulations confirmed an indirect (K-L) bandgap energy of 2.80 eV, with an electron transition between O-2p and Ce-4f orbitals, which agrees with the value obtained using diffuse reflectance. Raman spectroscopy shows that changing the synthesis times results in samples with different defect densities at a short range. Theoretical calculations confirmed that the deformations and changes in the experimental Raman spectra area result in oxygen displacement; as the displacement decreases, the crystallinity increases, and only one peak was observed. Scanning electron microscopy and high-resolution transmission electron microscopy show changes in the morphologies as the synthesis time varies. For shorter times, sheet and polyhedral morphologies were noted. With time increases, the sheets turn into nanorods and nanowires until the nanowires decrease and cubes are observed. In addition, an initial study regarding the influence of the surface on the electric response of CeO_2 was completed. It was observed that the presence of different surface defects ($[CeO_6{\cdot}2V_o^x]$ or $[CeO_7{\cdot}V_o^x]$) can alter the material resistance.

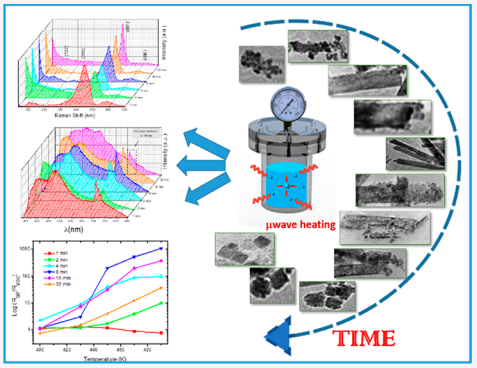

1. INTRODUCTION

Cerium oxide (CeO_2, ceria) is considered among the most important materials because of the great abundance of cerium (Ce) element in the rare earth element family and its capacity to release oxygen via Ce^{3+} to Ce^{4+} oxidation.[1] This material has several important technological applications, such as in solid oxide fuel cells (SOFCs),[2] ultraviolet absorbents,[3] photocatalysis,[4] optoelectronic devices,[5] glass polishing materials,[6] and biotechnology.[7] The latter application relies on ceria's low toxicity, chemical stability, unique redox property, high oxygen storage capability, and high oxygen mobility.[8]

Shape-selective synthesis of inorganic nanomaterials is of scientific and technological importance because of their unique shape-dependent material properties.[9−17] The morphological effect on the overall functionality of CeO_2 explains the importance of their shape-controlled synthetic strategy. Experimental and theoretical studies have confirmed that some CeO_2 nanocrystal properties are surface-structure-dependent.[18] The crystalline plane of ceria exerts a great influence on its properties. Sayle et al. used computer simulation techniques to model the surfaces of CeO_2 and paid special attention to the effects of surface structures and energetics on catalytic activity. The results showed that the (100) terminated surface is inherently more reactive and catalytically important as compared to those of the (111) and (110) surfaces. They also established that the (110) and (310) surfaces are more reactive in the oxidation of CO than (111) because of the formation of oxygen vacancies.[19] Stelmachowski et al. studied the effect of morphology, and therefore, the surface, on the catalytic total oxidation of methane. The author observed that the surface of the nanorod-type assemblies, using the hydrothermal method, has a superior catalytic response because of the Ce^{3+} presence.[20]

Controlled growth of CeO_2 nanostructures with a defined exposed surface, thus, is of substantial importance. In this sense, researchers have made efforts to synthesize various morphologies of CeO_2, including nanospheres, nanowires, nanotubes, nanorods, hollow/solid nanocubes, and nano-octahedrons, along with the investigation of their size- and shape-dependent performance.[12,16−18,21−29] A number of CeO_2 synthesis procedures, such as the precipitation,[30]

Received: February 10, 2020
Revised: July 1, 2020
Published: July 6, 2020

https://dx.doi.org/10.1021/acs.cgd.0c00165
Cryst. Growth Des. 2020, 20, 5031−5042

hydrothermal,[31] solvothermal[32] sol−gel,[33] and microwave-assisted methods,[34] were investigated.[20]

Concerning these methods, the microwave assisted hydrothermal (MAH) method has been regarded as among the most effective routes to achieve control of particle morphology, which can be done by controlling the temperature and time of synthesis, pH of the reaction medium, and use of surfactants, for example.[35−42] This synthesis method combines the benefit of both hydrothermal and microwave heating techniques and has advantages in comparison to those of the classical hydrothermal process because microwave irradiation increases the effective collision rate and reduces the time required to obtain isotropically grown nanostructures.[43] In addition, the MAH method is considered a single-step and low-temperature economical route for synthesis resulting in superior composition and powder reactivity. Araújo et al. used the MAH method to obtain CeO_2 nanoparticles of different morphologies. Morphology control was achieved by varying the synthesis temperature. Nanospheres evolved to nanorods with increasing synthesis temperatures.[37] Bezkrovnyi et al. prepared nanostructured three-dimensional (3D) CeO_2 nanocrystals via MAH synthesis. The authors studied the influence of synthesis conditions on the morphology and structure. The decisive effect of the OH^-/Ce^{3+} molar ratio in the reaction mixture on the size and shape of CeO_2 nanocrystals was established and explained. The authors observed a CeO_2 shape transformation from irregular (spheroidal) to cubical.[43]

In this paper, we report a facile synthesis procedure using the MAH method with simple precursors and without the addition of a surfactant to obtain different CeO_2 nanoparticle morphologies (wires, sheets, rods, and cubes) using synthesis time as the control parameter. A complete study of morphology and structure evolution of CeO_2 nanoparticle during the MAH method was performed. By varying the time of synthesis, keeping the temperature constant, it was possible to observe the morphological variation of the nanoparticles. The properties of the samples were studied by X-ray diffraction (XRD), Rietveld refinements, Raman ultraviolet−visible diffuse reflectance spectroscopies, and PL emissions. Field emission scanning electron microscopy (FE-SEM) and transmission electron microscopy (TEM) was employed to observe the morphologies of the nanocrystals. Electrical properties were studied by resistance measurements. Furthermore, periodic DFT calculations were made to complement the study of the properties of the equilibrium and defect structures. For the first time, an experimental and theoretical study of the relationship between the structural, optical, electronic, and electrical properties and morphology of CeO_2 nanomaterials is evaluated. These results may contribute to the area of synthesis of shape-selected ceria nanoparticles, and they allow us to understand how different morphologies and their transformations can affect the main properties of CeO_2 based materials.

2. EXPERIMENTAL SECTION

2.1. Synthesis. The synthesis of the CeO_2 particles was obtained using the MAH method. Cerium nitrate hexahydrate ($Ce(NO)_3 \cdot 6H_2O$, 99%, neon) and sodium hydroxide (NaOH, 97%, neon) were used. Initially, the $Ce(NO)_3 \cdot 6H_2O$, 0.06 M, was dissolved in 90 mL of 6 M NaOH and stirred for 1 h at room temperature, and a suspension formed. Subsequently, the suspension was transferred to the MAH system. After 20 min, the system has reached a temperature of 180 °C. This temperature is maintained for different time periods: 1, 2, 4, 8, 16, and 32 min. The obtained precipitates formed were collected at room temperature, washed with deionized water until the pH was neutralized, and dried in a conventional furnace at 70 °C for 5 h.

2.2. Characterization. Structural analyses of the samples were carried out via X-ray diffraction (XRD) using a diffractometer (model DMax/2500PC, Rigaku, Japan) with Cu Kα radiation (λ = 1.5406 Å) in the range of 20−92° and a scanning rate of 0.02°/min. The Rietveld refinements used the GSAS II program, using the card ICSD 239412, and a scan rate of 2°/min for a 2θ range of 10−110°. The Raman spectroscopy characterization was completed using a LabRAM iHR550 Horiba JobinYvon spectrometer equipped with a 514 nm laser as the excitation source with 1 cm^{-1} of spectral resolution. A total of 40 scans were performed from 50 to 800 cm^{-1}. Ultraviolet−visible light (UV−vis) diffuse reflectance spectra were obtained using a spectrophotometer (model Cary 5G, Varian, USA) in the diffuse reflection mode. The particle morphology was investigated using field-emission scanning electron microscopy (FE-SEM) on a Supra 35-VP Carl Zeiss, Germany, operated at 15 kV and high-resolution transmission electron microscopy (HR-TEM; TEM-FEI/PHILIPS CM120). Photoluminescence (PL) measurements were performed using a commercial confocal microscope (Attocube/CFMI). The samples were excited by a 355 nm laser coupled into a single mode optical fiber with the beam focused on the sample via an aspheric lens. The luminescence was collimated by the same lens and projected into a 50-μm multimode optical fiber dispersed by a 75 cm spectrometer (Andor-Shamrock) and detected using a charged couple device (AndoriDus).

To evaluate the temperature dependence of the resistance, the samples were pressed into pellets 8 mm in diameter and thermally treated at 380 °C/3 h (Figure S1). Notably, the pellets have the same shape with an identical distance between electrodes, and the only difference observed corresponds to the synthesis time. The resistance measurements were conducted at different temperatures from 330 to 490 K using a closed system at a pressure lower than 10^{-4} mbar and room pressure. Silver electrical contacts 100 nm in thickness were deposited on the pellets, which were obtained on an evaporator (model AUTO 306, Edwards) under the pressure of 10^{-7} mbar. Notably, the pellets have the same shape and the same distance between electrodes, and the differences between samples correspond only to the synthesis time. The resistance was determined using a Keithley 6517B electrometer.

2.3. Computational Methods. The CeO_2 structure in the thermodynamic equilibrium is cubic face-centered (CFC), belonging to the space group $Fm\bar{3}m$ with one Bravais lattice (a = 5.4124 Å). Its structure can be depicted as a cerium atom surrounded by eight oxygens, while each oxygen atom is coordinated by four cerium atoms (Figure 1). DFT simulations were completed using the CRYSTAL17

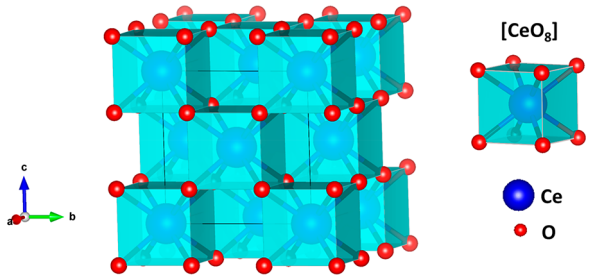

Figure 1. Schematic representation of CeO_2 crystalline unit cells.

package, where the WC1LYP (8% hybrid) was applied in common with an all-electron basis set of oxygen atoms (O_6-31d1)[44] and a pseudopotential basis set of cerium atoms.[45]

As a first procedure, the bulk optimizations of the CeO_2 structure were conducted to determine the equilibrium geometry. The electronic properties were analyzed through the band structure and the density of states (DOS), employing the same 20 k-point samplings as the diagonalization of the Fock matrix for the optimization process.

https://dx.doi.org/10.1021/acs.cgd.0c00165
Cryst. Growth Des. 2020, 20, 5031−5042

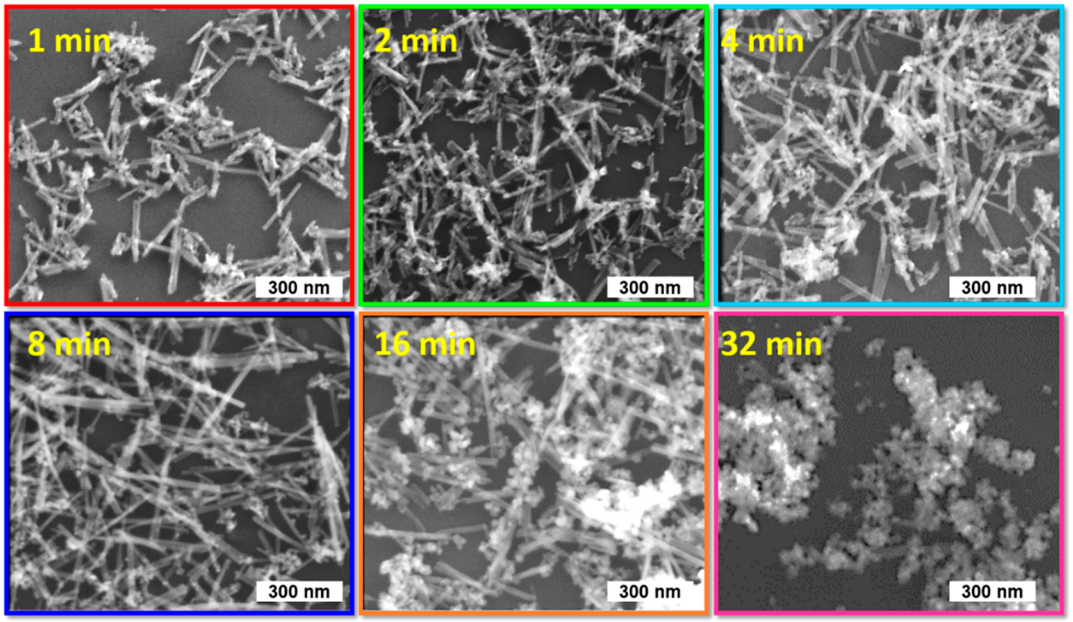

Figure 2. SEM images of CeO_2 prepared using the MAH method at a time variation of 1, 2, 4, 8, 16, and 32 min.

The surface stability and crystal morphologies were discussed by means of surface energy (E_{surf}) obtained by the following: $E_{surf} = E_{slab} - nE_{bulk}/2A$, where E_{slab} and E_{bulk} correspond to the optimized total energies of the surface and bulk, respectively; n is the number of CeO_2 units on each surface; and A is the surface area.

Additionally, the Raman theoretical spectra were obtained. The vibration frequencies at the Γ point were computed within the harmonic approximation by diagonalizing the mass-weighted Hessian matrix of the second derivatives of the total energy per cell with respect to the atomic displacements in the reference cell. More details regarding the computational vibration frequencies scheme can be found in the following ref 46.

The punctual defects can affect or even change the properties of the semiconductor materials. These defects modify the solid vibrational spectrum, and additional modes (local vibrational modes) appear, which can be detected by Raman spectroscopy and can be confirmed by theoretical calculations. In addition, the defects change the electronic level that can lead to the electrons being excited from or to these new levels; as a consequence, the return of these excited electrons to lower energy levels can entail to emitting light in different regions in the PL spectrum. Once experimentally determined, these defects depend on the use of various sophisticated equipment, and combining experimental research with theoretical research is essential for a conclusive analysis. In this sense, from the optimized bulk, displacements of 0.3, 0.2, and 0.1 Å on oxygen and cerium positions along the z-direction were completed to simulate structural defects.

3. RESULTS AND DISCUSSION

3.1. Morphological Analysis. *3.1.1. SEM and TEM Analyses.* The morphology of the particles obtained, using the MAH method, by varying the synthesis time between 1 and 32 min, was characterized by SEM (Figure 2) and TEM (Figure 3). The formation of sheet-like shapes, rods, wires, polyhedrons, and cubes, in different proportions, depending on the synthesis time was observed. As can be seen from the TEM and SEM figures, changes in morphology were more noticeable at longer synthesis times. However, in shorter synthesis times, it can be subtly observed that there is a transformation of sheets into wires and/or rods and simultaneously the formation of a larger number of polyhedrons. For the 1 min synthesis, Figure 3a1−a2 shows the formation of polyhedrons (with poorly defined faces) and sheet-like morphologies; notably, the sheets are of a greater proportion. Increasing the synthesis time (Figure 3b−d), it was observed that the sheets thinned and lengthened; thus, a gradual transformation of sheets into wires and/or rods can be observed and simultaneously the formation of a greater number of polyhedrons. As shown in Figure 3d, in the 8 min synthesis, there is a predominance of the wire-type morphology and a decrease in the polyhedral size. As the reaction continued, the nanoparticles agglomerated forming cubes, as shown in Figure 3e−f. For the 32 min synthesis, shown in Figure 3f, cubes were finally observed.

Using TEM images, we propose a growth and formation mechanism for the different CeO_2 morphologies (Figure 4). Because of the nanometric size, and therefore, the high surface energy of the particles, they initially tend to randomly agglomerate. As the synthesis time increases, the agglomerated particles organize themselves to form sheets. Increasing the system energy, the sheets are formed. Subsequently, the agglomeration is broken to form wires and rods. It can be seen that these rods/wires are also fragmented to form polyhedrons. These polyhedral agglomerates begin to form cubes, which are finally formed at a 32 min synthesis time.

In the literature,[36,43,47,48] there is a discussion regarding the mechanism of CeO_2 growth during MAH synthesis. However, in a general consensus, we can note that the growth of CeO_2 particles in a solution containing Ce^{3+} and OH^- ions involves a few steps. The first step is the solubilization of the ceria nitrate salt and the immediate formation of the Ce^{3+} ion. With the addition of OH^-, $Ce(OH)_3$ nuclei are rapidly formed because of the extremely low solubility. Then, the precipitates are easily oxidized to $Ce(OH)_4$ because of the existence of O_2 dissolved in the water during the magnetic stirring process. Next, the $Ce(OH)_4$ transforms into CeO_2 nuclei through a rapid oxidation and dehydration process. Since the $Ce(OH)_4$ phase was not found in the XRD, the oxidation and dehydration processes simultaneously occurred.

The CeO_2 nuclei during this stage are of small size and have poor crystallinity, high surface defects, and high surface energy;

https://dx.doi.org/10.1021/acs.cgd.0c00165
Cryst. Growth Des. 2020, 20, 5031−5042

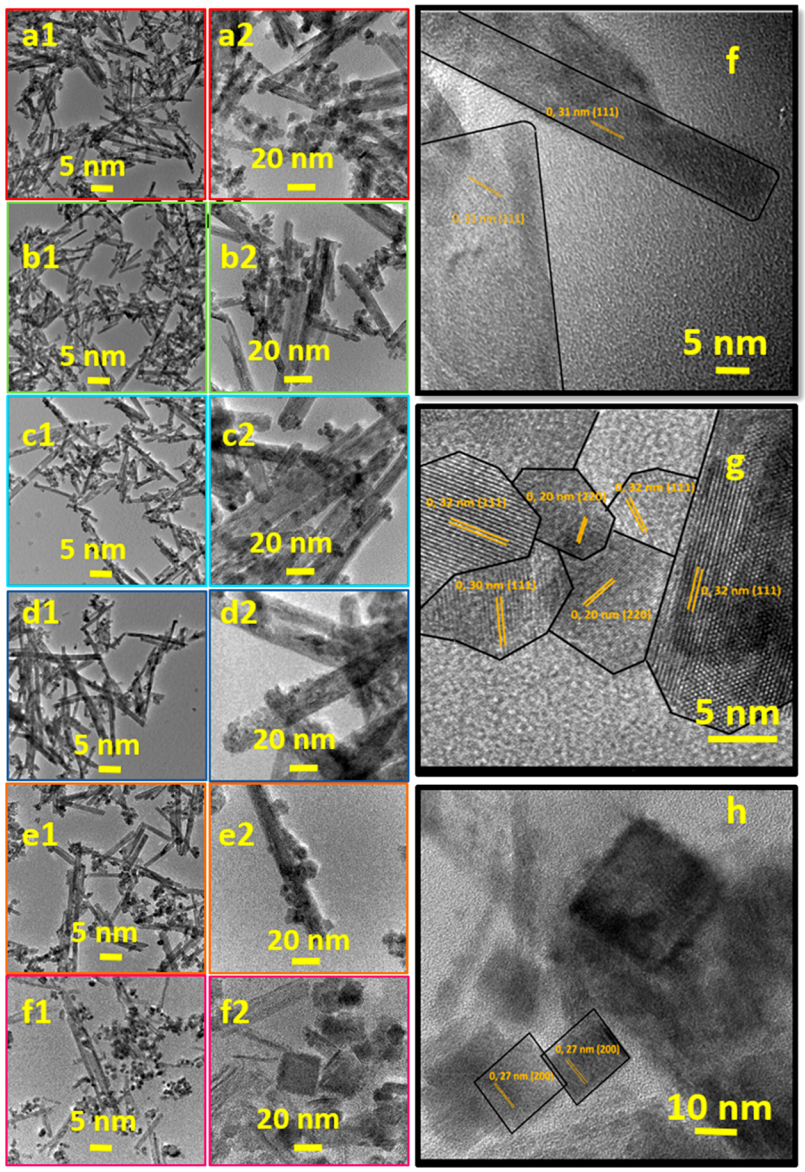

Figure 3. TEM images of CeO_2 prepared using the MAH method at a time variation of 1 (a1,2), 2 (b1,2), 4 (c1,2), 8 (d1,2), 16 (e1,2), and 32 (f1,2) min. HRTEM of the rods and sheets (f), polyhedrons (g), and cubes (h).

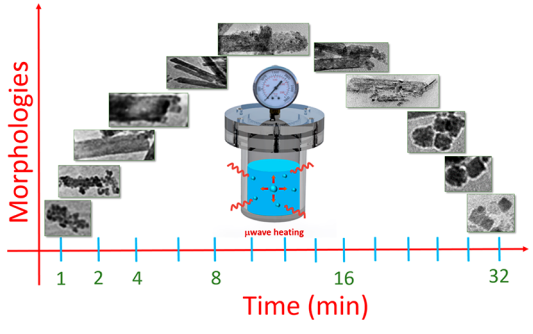

Figure 4. Proposed mechanism to explain the formation of different CeO_2 morphologies.

then, the agglomeration among nuclei tends to occur to reduce free energy, and therefore sheet-like nanostructures are formed. Here, two mechanisms for the hydrothermal conditions are proposed to explain the CeO_2 particle growth: oriented attachment (OA)[36,43,47] and Ostwald ripening (OR).[48] During the initial precipitation, the OA of nuclei occurs during the CeO_2 sheet formation. The OA occurs because of effective collision among nuclei with the same crystallographic orientation during the hydrothermal stage since the microwaves enhance nuclei dispersion and collision and promote the hydrothermal growth of CeO_2 and sheet formation.

Then, the OR process (dissolution−recrystallization) occurs to increase the crystallinity of the CeO_2 nanoparticles. Because of the low solubility of CeO_2 crystals in water, the OR process is an important key in the hydrothermal reactions of CeO_2 growth during this step, more crystals with defined morphologies can form via the dissolution of smaller nuclei. Increasing the synthesis time of microwave hydrothermal reactions, the OR process results in well-defined CeO_2 nanocrystal edges, and surface defects and surface energy are decreased. These may be the factors responsible for low interaction among the CeO_2 nanocrystals and disintegration of the sheet-like nanostructures and formation of more polyhedrons and cubes, as shown in Figures 2, 3, and 4.

https://dx.doi.org/10.1021/acs.cgd.0c00165
Cryst. Growth Des. 2020, 20, 5031−5042

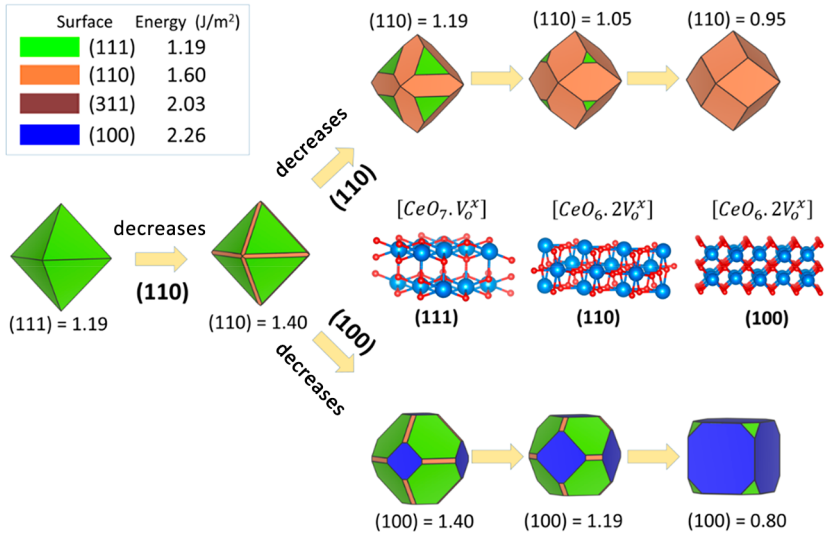

Figure 5. CeO_2 crystallographic structure and morphologies with crystalline planes (111), (110), (311), and (100). In the middle of the image is the representation of the defect types present in the (111), (110), and (100) surfaces.

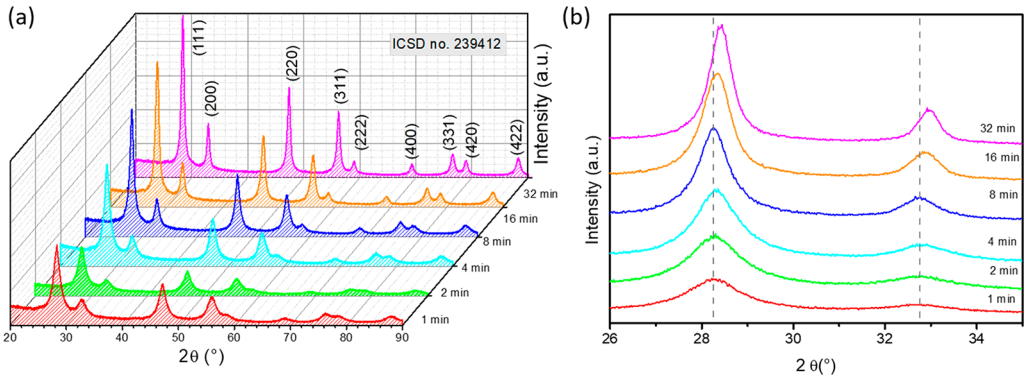

Figure 6. (a) XRD patterns of CeO_2 prepared using the MAH method by time variation of 1, 2, 4, 8, 16, and 32 min. (b) XRD approximation.

TEM analyses were also performed to better elucidate the morphologies resulting from the nanometric nature of CeO_2 particles and to identify an explanation for the observed particle crystalline structure. As shown in Figure 3f, related to the 1 min sample, sheets and wires occur: both structures present a lattice spacing of 0.31 nm corresponding to the (111) plane. Figure 3g, related to the 4 min sample, shows polyhedron and rod morphologies. The rods have a lattice spacing of 0.31 nm corresponding to the (111) plane. The polyhedrons show two different lattice spacing values: 0.32 and 0.20 nm, which correspond to the (111) and (220) planes, respectively. Figure 3h, related to the sample synthesized at 32 min, shows a high-resolution image of CeO_2 cubes that have a lattice spacing of 0.27 nm corresponding to the (200) plane.

According to the literature, there are three low-index lattice planes on the surface of CeO_2 nanocrystals: (100), (110), and (111). For these surfaces, the coordination numbers are less than in the bulk (8 for Ce^{4+} and 4 for O^{2-}), which indicates more active surfaces. Experimental and theoretical studies have confirmed that the vacancy formation energy is different for these surfaces following the order of (110) < (100) < (111).[49]

Our theoretical results, consistent with the literature, allowed us to determine a set of morphologies for CeO_2 as shown in Figure 5. The transformation of the morphologies can be obtained by changing the ratio between the E_{surf} values for each surface. The surface energy can be altered because of geometric constraints imposed on the crystalline structure.[50] The crystalline morphologies grow from the ideal crystal, (111) with E_{surf} = 1.19 J/m^2; thus, the facets (111) are the main ones exposed to minimize the surface energy. Notably, with the decrease in the E_{surf} (100), a cube morphology begins to form, and with a decrease in the E_{surf} (110) the morphology tends to conform as polyhedra, which are consistent with the results shown in Figure 7 for the exposed crystalline planes for cubes and polyhedra. The experimental morphologies nanosheets, nanorods, and nanowires can be correlated to the theoretical ones considering the decrease in the E_{surf} of planes (111) and (110) as well as the defects present along the synthesis route.[51] Different types of defects are found for each exposed surface as shown in the middle of Figure 5, and therefore the nanorods, nanowires, nanopolyhedra, and nanocubes have different defect densities.

The formation of oxygen vacancies and other lattice defects is very important for oxygen anion mobility.[7] As the number of vacancies increases, the movement of oxygen atoms is facilitated in the crystal. The increased oxygen diffusion rate in the lattice during synthesis causes modifications not only in the optical properties but also influences the electrical properties as will be shown in the electrical resistance analyses.

3.2. XRD Patterns and Rietveld Refinements. Figure 6a shows the XRD patterns of CeO_2 prepared using the MAH method by time variation of 1, 2, 4, 8, 16, and 32 min. All

https://dx.doi.org/10.1021/acs.cgd.0c00165
Cryst. Growth Des. 2020, 20, 5031−5042

Table 1. Results Obtained from Rietveld Refinements of CeO_2 Powders

synthesis time (min)	$a = b = c$ (Å)	V (Å^3)	crystallite size (mkm)	dist. bond Ce1−O1 (Å)	microstrain ($\mu\varepsilon$)	wR (%)
1	5.45	161.74	0.044	2.36(0)	63296.72	5.56
2	5.44	161.39	0.058	2.36(0)	76341.26	6.13
4	5.44	161.17	0.081	2.35(0)	38230.00	5.79
8	5.46	162.62	0.086	2.36(0)	23830.02	6.11
16	5.43	160.52	0.018	2.35(0)	14260.00	5.91
32	5.43	160.01	0.019	2.36(0)	59387.55	6.58

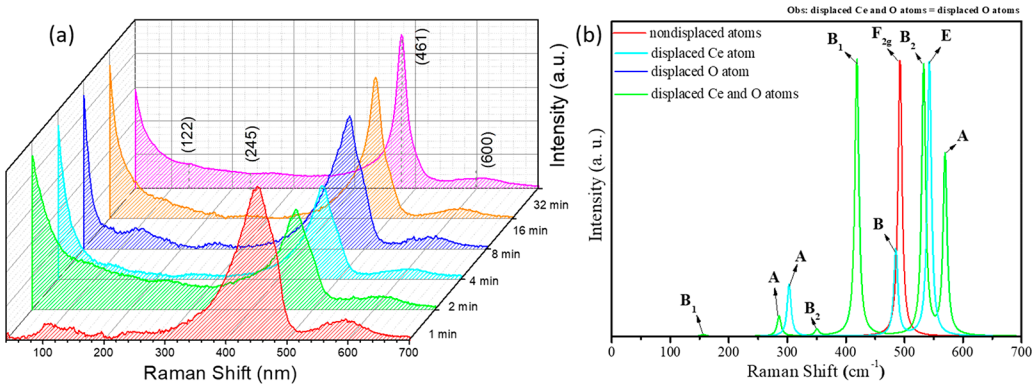

Figure 7. (a) CeO_2 Raman spectra of CeO_2 prepared using the MAH method by time variation (b) CeO_2 theoretical Raman.

reflections were assigned to the cubic structure of CeO_2 belonging to the space group $Fm\bar{3}m$ (ICSD pattern no. 239412). The corresponding Miller indices were provided, and no additional reflections were found, which suggests high phase purity. All of the CeO_2 reflections are broad because of the nanometric crystalline size and lattice microstrain, serving as a measure of lattice defects. In addition, it was observed that when increasing the synthesis time the reflections become progressively narrower and sharper; the intensity gradually increases, while the width at half height decreases, indicating that the long-range symmetry and crystallinity of CeO_2 were enhanced.

Figure 6b shows the XRD peak shift for the CeO_2 nanostructures obtained at different synthesis times. For the samples with longer synthesis times (16 and 32 min), a shift to a greater angle of the diffracted peak is observed. This displacement may be associated with the composition or parameters of the crystalline lattice such as volume[52] or stress.[53] Here, the displacement to higher angles is associated with the lattice tensile stress, which is related to the change in particle morphology with synthesis time.

To better compile the XRD results, Rietveld refinement of the diffractograms was performed as presented in Table 1 and Figure S2. The fitting parameters (wR (%)) indicate good agreement between the calculated and observed XRD patterns for the as-prepared CeO_2 nanocrystals. For this, was used the GSAS-II programs and the ICSD (Inorganic Crystal Structure Database) number 239412 published in ref 54 were employed. In this crystallographic sheet, CeO_2 has a lattice parameter value of 5.4665 Å. The lattice parameter value presented by our samples is in agreement with this article, and several others presented in the literature.[55−60] A review of the ICSD databases showed that the CeO_2 lattice parameters could range from 5.38 to 5.52 Å, according to the ICSD cards 28709 and 165720, respectively. Moreover, it can be observed that these parameters significantly change with the synthesis time, which may be associated with modifications in the nanoparticle morphology, crystallinity, and straining due to the particle synthesis time. Higher values of the crystalline parameters are observed for the nanoparticles obtained with 8 min; this is related to the predominance of the type of morphology and consequent type of defect in the structure.[61,62]

However, the 32 min sample of synthesis with the crystallization and recrystallization retains growth and results in the lower lattice parameter value.

Rietveld refinement indicated that in the CeO_2 unit cell the lattice former Ce is surrounded by eight oxygens to form [CeO_8] clusters. An analysis of the values for the bond distances on the [CeO_8] clusters was performed, and the results are shown in Table 1. It can be seen that these clusters present different bond distances and microstrain values, and thus a displacement from the original position can be determined. These results indicate lattice distortions and structural defects, which cause polarization and symmetry breaking and therefore the formation of different defect densities.[63] In addition, these defects enhance the charge transfer (CT) process among the clusters, from which the material properties such as PL and conductivity arise. Regarding the crystalline size, it has a tendency to increase according to the time of synthesis for the samples up to 8 min and then a reduction for samples obtained at 16 and 32 min, which is in agreement with variations in lattice parameters for oriented particle growth.[64]

The theoretical calculation obtained a cell parameter (a) value of 5.39 Å; this value is nearer the a for the CeO_2 nanocrystal synthesized at 32 min (5.43 Å) determined by the Rietveld refinement (see Table 1) with a small deviation (0.66%). The theoretically calculated values of the volume and bond distance Ce−O were 156.84 Å^3 and 2.34 Å, respectively. All the theoretical results are in accordance with the CeO_2 nanocrystal synthesized experimental data. However, the proximity to the results of the CeO_2 nanocrystal after 32 min of synthesis is because of the high crystallinity obtained

https://dx.doi.org/10.1021/acs.cgd.0c00165
Cryst. Growth Des. 2020, 20, 5031−5042

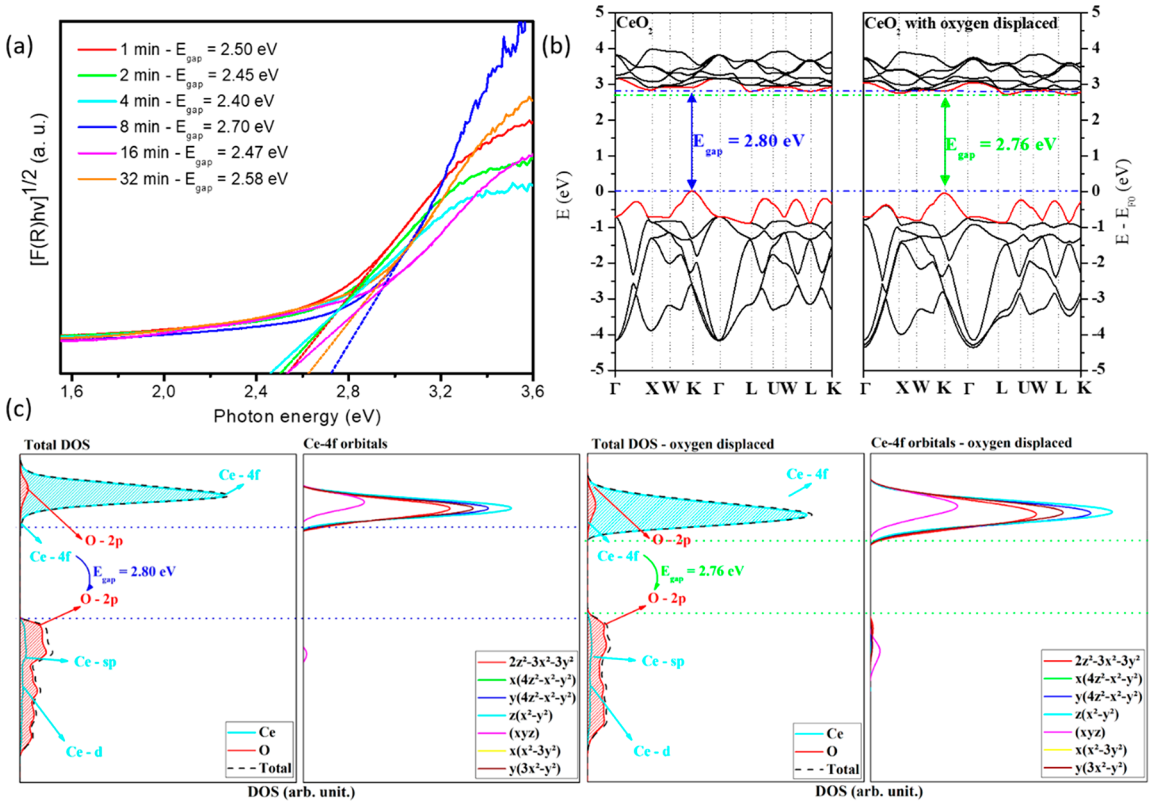

Figure 8. (a) Diffuse reflectance spectra of CeO_2 prepared using the MAH method at a time variation of 1, 2, 4, 8, 16, and 32 min. (b) Energy bands and (c) partial DOS of CeO_2 without and with oxygen displaced.

over this time, once the theoretical simulation considered the crystal without any defects.

3.3. Raman Spectroscopy. Raman spectroscopy can be employed to determine the short-range order−disorder relationship in semiconductor materials, which, in our case, can be used to analyze the local coordination of Ce clusters as constituents of CeO_2 crystals. Figure 7a shows the Raman spectra of CeO_2 nanostructures at the excitation wavelength of 325 nm. According to the literature, CeO_2 nanoparticles show one strong intense band at 461 cm^{-1} that generally corresponds to the active triply degenerated F_{2g} Raman active-mode of fluorite type cubic structure because of the symmetric breaking mode of the oxygen atoms around the cerium ions. The Raman spectrum thus corroborates that the synthesized products have a crystalline fluorite cubic structure.[65] However, three additional peaks at ∼600, 245, and 122 cm^{-1} were observed, which may be associated with short-range structural defects. The main defect in CeO_2 nanocrystals is the formation of oxygen vacancies.[66,67] In the fluorite structure, the oxygen atoms are all in the same plane, allowing rapid diffusion as a function of the number of oxygen vacancies.[68] Oxygen vacancies can be produced via the following defect reaction between Ce^{3+} and Ce^{4+}, via the interaction between ordered and disordered clusters. The oxygen vacancies in a disordered structure $[CeO_8]_d^x$ can also be represented as $[CeO_8]_d^x/[CeO_7{\cdot}V_o^x]$ complex clusters and can be considered hole-trapping centers according to the following equations that consider the intrinsic generation of defects at clusters:

$$[CeO_8]_o^x ... [CeO_8]_d^x \leftrightarrow [CeO_8]_o^x ... [CeO_7{\cdot}V_o^x] + 1/2\, O_2 \quad (1)$$

$$[CeO_8]_o^x ... [CeO_7{\cdot}V_o^x] \leftrightarrow [CeO_8]_o' ... [CeO_7{\cdot}V_o^{\bullet}] \quad (2)$$

$$[CeO_8]_d^x ... [CeO_7{\cdot}V_o^{\bullet}] \leftrightarrow [CeO_8]_o' ... [CeO_7{\cdot}V_o^{\bullet\bullet}] \quad (3)$$

where V_o^x represents is the neutral vacancy, and $V_o^{\bullet}$ and $V_o^{\bullet\bullet}$ are the singly and doubly ionized vacancies, respectively. Thus, these three bands can be linked to lattice defects, which result in oxygen vacancy creation.

With increasing synthesis time, the modes thin, the width at half height decreases, and the three additional peaks at ∼600, 245, and 122 cm^{-1} disappear, indicating an increase in the structural order at a short range. This characteristic is associated with the kinetics under synthesis conditions and also the intrinsic lattice structural order as was confirmed by the Rietveld refinement. Moreover, it was observed that the modes have different widths at half-height values. Therefore, it can be stated that the increase in synthesis times leads to significant differences in the formation of short-range defects in the CeO_2 crystals.

The obtained theoretical Raman spectra are shown in Figure 7b, and the only band at 491 cm^{-1}, characterized by the F_{2g} Raman active mode, confirms the high pure experimental nanocrystal with a deviation of 6.51%. However, to analyze the deformations and changes in the Raman spectra observed at other time synthesis times, different distortions were simulated on the structure through the displacement of atoms along the *z*-direction. In this sense, a displacement of 0.3 Å on O, Ce, and both (O and Ce at the same time) was made. As can be seen in Figure 7b, when the O and both Ce and O were displaced, the same active modes were found, while for the displacement only in the Ce atom, the modification is not significant. In particular, the mode at ∼151 cm^{-1} only appears

https://dx.doi.org/10.1021/acs.cgd.0c00165
Cryst. Growth Des. 2020, 20, 5031−5042

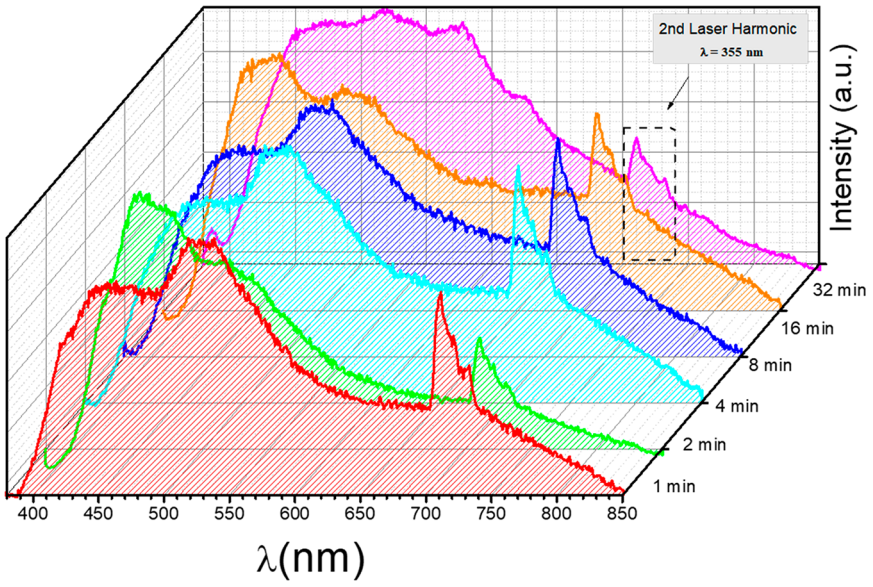

Figure 9. PL of CeO_2 prepared using the MAH method at a time variation of 1, 2, 4, 8, 16, and 32 min.

when the oxygen atom is displaced and also appears in the experimental Raman spectrum for the syntheses less than 32 min. Therefore, these results show that the structural distortions were caused by the oxygen displaced on the crystalline cell. Analyzing only the displaced oxygen, two additional displacements along the *z*-direction were made completed of 0.1 and 0.2 Å. These models were compared with the 0.3 Å displaced model and with a no displaced atom to investigate the degree of the defects observed in the experimental Raman spectrum. The analysis showed that as there is an increase in structural defects, caused by the oxygen displacement, new active modes appear and become more spaced from one another. In contrast, when the structural defects are minimized, the active modes approach the defect-free model, generating only one mode at 491 cm^{-1}. Therefore, this analysis showed not only the cause of the structural defects experimentally observed but also confirmed the major degree of crystallinity obtained in the sample at 32 min.

3.4. Ultraviolet−Visible Light Diffuse Reflectance Spectroscopy. Figure 8a shows the UV-Vis diffuse reflectance spectra of the CeO_2 nanocrystals. The CeO_2 crystals show an optical diffuse reflectance spectrum governed by indirect electronic transitions; on the basis of this, the band gap energy (E_{gap}) values of the CeO_2 nanocrystals were calculated using the methods proposed by Kubelka and Munk[69] and Wood and Tauc[70] and were determined by extrapolating the linear portion of the UV−Vis curve. As shown in Figure 8a, there is an E_{gap} between 2.5 and 2.7 eV. These values are similar to those reported in the literature.[71−73]

According to the band structure shown in Figure 8b, the theoretical band gap is indirect, and it occurs between the K-L k-points (2.80 eV) and agrees well with the present experimental value and literature data. The density of states (DOS) analysis (Figure 8c) shows that the major contributor of the band gap is the O-2p level at VB (the three p components equally contribute), and there is also a contribution of Ce-$f_{(x^2-y^2)z}$ above the Fermi level (E_F) at CB, which is characterized as the O_{2p}-Ce_{4f} gap. A second band gap can be observed considering the electron transition between O_{2p}-Ce_{5d}, in which Ce-$5d_{(x^2-y^2)}$ is the major contributor from 10.05 eV, given a band gap of the same value. Despite the great accordance between the experimental and theoretical main band gap values, the WC1LYP overestimates the second band gap, and the obtained value is greater than that experimentally obtained in the present work and available in the literature.[45] The two band gaps discussed in the present work were previously theoretically discussed by Sanz and co-workers,[45] and the results obtained here are in accordance with theirs.

The band structure and DOS of the model with the oxygen atom displaced by 0.1 Å are shown in Figure 8c; this is the distorted model that represents the experimental morphology with structural defects. Compared to the case of the nondisplaced model, it can be seen that with the oxygen displaced the orbitals at valence bands were conserved, and only the electronic levels above E_F were displaced downward. However, as the Ce-f orbital is the most significant contributor above E_F (CB), this orbital was also displaced, along with the displacement of the O-2p orbitals. Thus, the reduction in the band gap (O_{2p}-Ce_{4f}) observed is because of the displacement of the electronic levels above the Fermi energy and not of the valence band. In addition, no significant change was observed in the behavior of the band structures with the simulated structural defect.

3.5. PL Emissions. The PL profiles for the CeO_2 nanocrystals measured using a 355 nm Cobolt/Zoukas an excitation source are shown in Figure 9.The CeO_2 spectrum originates from the defect states extensively occurring between the Ce 4f state and O 2p valence band.[74] The broadband profile of the PL emission band is typical of a multiphonon and multilevel process; this behavior is reported in a system in which relaxation occurs by several paths, involving the participation of numerous states within the band gap of the material with disorder/defects in the lattice.[75] These defects possibly act as radiative recombination centers for electrons initially excited from the valence band to the 4f band of the CeO_2.[74]

It is also observed in Figure 9 that the broadband PL reaches frequencies ranging from violet to red. The photoluminescence influence in different regions of the visible spectrum is associated with the different routes traveled by the charge

https://dx.doi.org/10.1021/acs.cgd.0c00165
Cryst. Growth Des. 2020, 20, 5031−5042

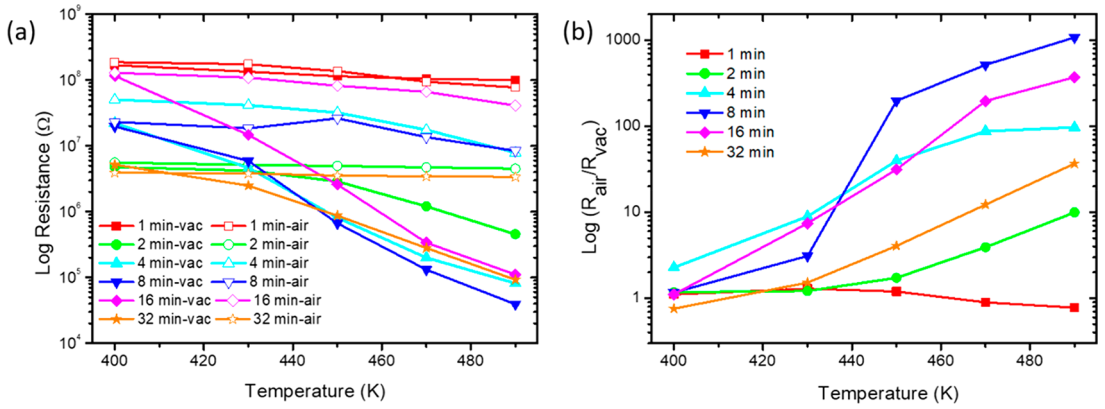

Figure 10. (a) Resistance versus temperature for CeO_2 particles obtained at 1, 2, 4, 8, 16, and 32 min measured in air and 10^{-5} mbar (vacuum) and room pressure. (b) Ratio of resistance in air to the resistance in the vacuum.

carrier during exciton recombination (electron−hole pair). The broadband from approximately 400 to 850 nm has four evident emission bands: a blue broad emission band at ∼445 nm (2.79 eV), blue-green band at 460 nm (2.70 eV), yellow-red band at ∼515 nm (2.41 eV), and red band at 530 nm (2.34 eV).

It can be observed that with the increase in the synthesis time, the samples show different PL profiles. This indicates that different synthesis times causes particle formation with different sets of defects. This may be associated with the crystallization−dissolution−recrystallization process that occurs within the microwave reactor during CeO_2 nanoparticle growth, which provokes distortion in the hexahedron $[CeO_8]$ clusters at medium range and changes in the morphologies. These distortions on the $[CeO_8]$ clusters aid the formation of intermediary energy levels within the band gap of this material that provokes nonlinear variations in the PL intensity of the CeO_2 nanocrystals obtained using the MAH process. In addition, this behavior can be associated with the formation of superficial defects caused by modifications of the morphology of these powders. Thus, the morphology modifications of different planes and surfaces, with dissimilar sets of defects, are exposed. These defects originate from rapid heating, high effective collision rates between the small particles, and growth processes during the processing of CeO_2 nanoparticles. Therefore, using the different synthesis times in the MAH method, one can produce samples with different densities of defects and, therefore, unique properties.

3.6. Electrical Properties. To understand the electron transport properties of CeO_2 synthesized particles with different morphologies, resistance versus temperature behavior is shown in Figure 10. Because semiconductor oxides present a remarkable change in the electrical properties when exposed to O_2, CO, and NO_2 gases,[76] for the purposes of this study, electrical resistance dependence on the atmosphere was also assessed. Samples were also evaluated in a vacuum (10^{-4} mbar) and dry air atmospheres. When samples are exposed to air, the oxygen interaction with the clusters should be considered. Ceria disordered structures (represented as clusters interacting with O_2) interact with air and can be represented in the following equations (4−7):[77]

$$[CeO_7\cdot V_o^x] + O_2 \leftrightarrow [CeO_7\cdot V_o^x]...O_2\ (\text{ads}) \quad (4)$$

$$[CeO_6\cdot 2V_o^x] + O_2 \leftrightarrow [CeO_6\cdot 2V_o^x]...O_2\ (\text{ads}) \quad (5)$$

$$[CeO_7\cdot V_o^x]... O_2 \leftrightarrow [CeO_7\cdot V_o^{\cdot}]...O_2'\ (\text{ads}) \quad (6)$$

$$[CeO_6\cdot 2V_o^x]...O_2 \leftrightarrow [CeO_6\cdot V_o^x V_o^{\bullet}]...O_2'\ (\text{ads}) \quad (7)$$

From the obtained results shown in Figure 10a, the electrical transport characteristics of the CeO_2 nanoparticles agree with an n-type semiconductor behavior, in which the exposure to a dry air atmosphere increases the sample resistance. For the following interpretations, we must consider that the electrical resistance depends on different factors such as grain boundary, particle size, and in the case of CeO_2, the presence of free electrons at the cerium $4f^1$ states as a result of ionized vacancy formation (eqs 4−7).[78] In this work, the resistance dependence on temperature and gas atmosphere must also be related to the sample morphology obtained as a result of the different synthesis times. From Figure 10a, when samples were exposed to a vacuum atmosphere, the electrical resistance decreased with temperature depending on different surfaces (obtained with the synthesis time). The vacuum promotes oxygen desorption at the sample surface (inverse of eqs 6 and 7). Then, a decrease in the electrons at the 4f cerium state promotes a decrease in the sample resistance because of the elimination of $O_2^{\cdot}$.

Electrical measurements were conducted, and in a vacuum atmosphere at temperatures above 430 K, an electrical resistance decrease was observed for the samples obtained up to 8 min of synthesis (Figure 10a); a slight decrease in resistance for samples with a synthesis time of 16 and 32 min was noted. There are different surfaces in all morphologies; however, at the synthesis time of 8 min, more wire was observed which dominated the surface (111). In the surface (111), there is only one vacancy because of the presence of the $[CeO_7\cdot V_o^x]$ cluster, while on surfaces (100) and (110) two vacancies occur, because of the presence of the $[CeO_6\cdot 2V_o^x]$ cluster. When there is only one vacancy, the holes formed are more stable, which reduces the electrical resistance. In the other samples, there is a predominance of surfaces (100) and (110), with two vacancies, in which there is a resonance between the vacancies stabilizing the interaction electron/role ($V_o^x\ V_o^{\bullet} \leftrightarrow V_o^{\bullet}V_o^x$).

Previous studies have shown that the electric conduction of undoped CeO_2 particles is dominated by a tunneling current,[77] in which defects are created because of the presence of an oxygen vacancy, $[CeO_7\cdot V_o^x]$, allowing an increase in the number of electrons at the 4f cerium states. When the $4f^0$ states receive an electron from the vacancy formation process,

https://dx.doi.org/10.1021/acs.cgd.0c00165
Cryst. Growth Des. 2020, 20, 5031−5042

an electrical resistance decrease is observed.[78] Analyzing the R_{air}/R_{vac} ratio, shown in Figure 10b, it is observed that the slope of the curve increases for the samples obtained from 1 to 8 min of synthesis with the maximum slope observed for the 8 min sample. The R_{air}/R_{vac} ratio decreases for the 16- and 32 min samples. The largest slope is the result of the greatest difference in resistance between the vacuum and dry air exposure. This means that O_2 molecules present in atmospheric air are adsorbed onto the CeO_2 surface and result in electron trapping[79,80] with a greater effect for the sample obtained with 8 min of synthesis. We attribute this effect to wire morphologies with a predominance of $[CeO_7{\cdot}V_o^x]$ defects. After 8 min of synthesis, wire-like morphologies begin to fragment increasing polyhedral and cubic morphology formation and consequently an increase in the $[CeO_6{\cdot}2V_o^x]$ defects. Therefore, the connectivity between the wire type particles and the increase in $[CeO_7{\cdot}V_o^x]$ defects tends to improve the material sensitivity when the atmosphere is changed from air to a vacuum.

4. CONCLUSIONS

In this work, CeO_2 nanocrystals were successfully synthesized using the MAH method, and, for the first time, the effects of synthesis time on the crystalline structure, morphology, and optical properties were investigated. First-principle calculations at the DFT level provided a comprehensive knowledge of the electronic and structural properties. The main conclusions are summarized as follows: (i) The XRD patterns and Rietveld refinement data showed that all CeO_2 samples were crystallized in the fluorite-type cubic structure. (ii) Raman spectroscopies confirmed the presence of the F_{2g} active mode characteristic of the CeO_2 cubic structure; in addition, unexpected modes were observed. The theoretical calculations showed that the appearance of new peaks was due the displaced oxygen as confirmed by the theoretical Raman spectra. In addition, with an increase in the synthesis time, these extra peaks disappeared, confirming an increase in the symmetry at a short range. (iii) The SEM images showed that the synthesis temperature influences the shape of the CeO_2 nanocrystals, which initially exhibit sheet and polyhedral morphologies. With increasing synthesis time, the sheets turned into nanorods and nanowires, and the proportion of polyhedral structures increased until the nanowires decreased and cubes were observed. (iv) The UV−vis spectra showed indirect transitions. The theoretical indirect band gap occurs between O_{2p} and Ce_{4f}, and this agrees with the experimental data. In addition, the model with oxygen displaced simulating an oxygen defect in the cell shows that the band gap decrease was according to the level above E_F, which corresponds to the Ce_{4f} orbitals. (v) Finally, it was found that the increase in sample sensitivity is an effect produced as a consequence of the increasing oxygen vacancies. The effect was a change in the morphologies, and consequently, exposed planes can be used for tuning the band gap and oxygen sensitivity, which is useful for optoelectronic device fabrication and sensing properties.

■ ASSOCIATED CONTENT

Supporting Information

The Supporting Information is available free of charge at https://pubs.acs.org/doi/10.1021/acs.cgd.0c00165.

SEM image of pellets and Rietveld refinement of CeO_2 samples (PDF)

■ AUTHOR INFORMATION

Corresponding Author

Regiane Cristina de Oliveira − *Faculty of Engineering of Guaratinguetá and Modeling and Molecular Simulation Group, São Paulo State University - UNESP, Guaratinguetá, São Paulo, Brazil;* orcid.org/0000-0002-7332-8731; Email: g.ianeoliveira@hotmail.com

Authors

Rafael Aparecido Ciola Amoresi − *Faculty of Engineering of Guaratinguetá, São Paulo State University - UNESP, Guaratinguetá, São Paulo, Brazil;* orcid.org/0000-0002-7523-6013

Naiara Letícia Marana − *Modeling and Molecular Simulation Group, São Paulo State University - UNESP, Bauru, São Paulo, Brazil*

Maria Aparecida Zaghete − *Interdisciplinary Laboratory of Electrochemistry and Ceramics, LIEC − Chemistry Institute, São Paulo State University - UNESP, Araraquara, São Paulo, Brazil*

Miguel Ponce − *Research Institute of Materials Science and Technology, INTEMA - National University of Mar del Plata, Mar del Plata, Argentina*

Adenilson José Chiquito − *NanOLaB - Department of Physics, Federal University of São Carlos, UFSCar, São Carlos, São Paulo, Brazil*

Julio Ricardo Sambrano − *Modeling and Molecular Simulation Group, São Paulo State University - UNESP, Bauru, São Paulo, Brazil;* orcid.org/0000-0002-5217-7145

Elson Longo − *Interdisciplinary Laboratory of Electrochemistry and Ceramics, LIEC - Federal University of São Carlos, UFSCar, São Carlos, São Paulo, Brazil;* orcid.org/0000-0001-8062-7791

Alexandre Zirpoli Simões − *Faculty of Engineering of Guaratinguetá, São Paulo State University - UNESP, Guaratinguetá, São Paulo, Brazil*

Complete contact information is available at: https://pubs.acs.org/10.1021/acs.cgd.0c00165

Notes

The authors declare no competing financial interest.

■ ACKNOWLEDGMENTS

The authors thank the São Paulo Research Foundation (FAPESP) under CEPID/CDMF grants (#2008/57872-1, #2013/07296-2,#2016/07476-9, #2016/25500-4, and #2017/19143-7) and the National Council for Scientific and Technological Development (CNPq) (#573636/2008-7) for their financial support in the course of this research. Research supported by LNLS - Brazilian Synchrotron Light Laboratory, Research LMF - 24859, CNPEM/MCTIC. This study was financed in part by the Coordenação de Aperfeiçoamento de Pessoal de Nível Superior − Brasil (CAPES) − Finance Code 001. We also acknowledge Professor Marcio Daldin Teodoro for the photoluminescence measurements.

■ REFERENCES

(1) Sun, C.; Li, H.; Chen, L. Nanostructured ceria-based materials: synthesis, properties, and applications. *Energy Environ. Sci.* **2012**, *5*, 8475.

(2) Yahiro, H.; Baba, Y.; Eguchi, K.; Arai, H. High Temperature Fuel Cell with Ceria-Yttria Solid Electrolyte. *J. Electrochem. Soc.* **1988**, *135*, 2077−2081.

(3) Fang, Q.; Liang, X. CeO_2−Al_2O_3, CeO_2−SiO_2, CeO_2−TiO_2 core-shell spheres: formation mechanisms and UV absorption. *RSC Adv.* **2012**, *2*, 5370.
(4) Tian, J.; Sang, Y.; Zhao, Z.; Zhou, W.; Wang, D.; Kang, X.; Liu, H.; Wang, J.; Chen, S.; Cai, H.; Huang, H. Enhanced photocatalytic performances of CeO_2/TiO_2 nanobelt heterostructures. *Small* **2013**, *9*, 3864−3872.
(5) Wang, Z.-L.; Li, G.-R.; Ou, Y.-N.; Feng, Z.-P.; Qu, D.-L.; Tong, Y.-X. Electrochemical Deposition of Eu^{3+}-Doped CeO_2 Nanobelts with Enhanced Optical Properties. *J. Phys. Chem. C* **2011**, *115*, 351−356.
(6) Feng, X. Converting Ceria Polyhedral Nanoparticles into Single-Crystal Nanospheres. *Science* **2006**, *312*, 1504−1508.
(7) Ji, Z.; Wang, X.; Zhang, H.; Lin, S.; Meng, H.; Sun, B.; George, S.; Xia, T.; Nel, A. E.; Zink, J. I. Designed Synthesis of CeO_2 Nanorods and Nanowires for Studying Toxicological Effects of High Aspect Ratio Nanomaterials. *ACS Nano* **2012**, *6*, 5366−5380.
(8) He, H.; Yang, P.; Li, J.; Shi, R.; Chen, L.; Zhang, A.; Zhu, Y. Controllable synthesis, characterization, and CO oxidation activity of CeO_2 nanostructures with various morphologies. *Ceram. Int.* **2016**, *42*, 7810−7818.
(9) Mai, H.-X.; Sun, L.-D.; Zhang, Y.-W.; Si, R.; Feng, W.; Zhang, H.-P.; Liu, H.-C.; Yan, C.-H. Shape-Selective Synthesis and Oxygen Storage Behavior of Ceria Nanopolyhedra, Nanorods, and Nanocubes. *J. Phys. Chem. B* **2005**, *109*, 24380−24385.
(10) Feng, Z.; Ren, Q.; Peng, R.; Mo, S.; Zhang, M.; Fu, M.; Chen, L.; Ye, D. Effect of CeO_2 morphologies on toluene catalytic combustion. *Catal. Today* **2019**, *332*, 177−182.
(11) Cao, T.; You, R.; Li, Z.; Zhang, X.; Li, D.; Chen, S.; Zhang, Z.; Huang, W. Morphology-dependent CeO_2 catalysis in acetylene semihydrogenation reaction. *Appl. Surf. Sci.* **2020**, *501*, 144120.
(12) Yan, D.; Mo, S.; Sun, Y.; Ren, Q.; Feng, Z.; Chen, P.; Wu, J.; Fu, M.; Ye, D. Morphology-activity correlation of electrospun CeO_2 for toluene catalytic combustion. *Chemosphere* **2020**, *247*, 125860.
(13) Li, X.; Feng, J.; Perdjon, M.; Oh, R.; Zhao, W.; Huang, X.; Liu, S. Investigations of supported Au-Pd nanoparticles on synthesized CeO_2 with different morphologies and application in solvent-free benzyl alcohol oxidation. *Appl. Surf. Sci.* **2020**, *505*, 144473.
(14) Li, S.; Zhang, Y.; Wang, Z.; Du, W.; Zhu, G. Morphological Effect of CeO_2 Catalysts on Their Catalytic Performance in Lean Methane Combustion. *Chem. Lett.* **2020**, *49*, 461−464.
(15) Yang, S.; Zhou, F.; Liu, Y.; Zhang, L.; Chen, Y.; Wang, H.; Tian, Y.; Zhang, C.; Liu, D. Morphology effect of ceria on the performance of CuO/ CeO_2 catalysts for hydrogen production by methanol steam reforming. *Int. J. Hydrogen Energy* **2019**, *44*, 7252−7261.
(16) Zheng, H.; Hong, Y.; Xu, J.; Xue, B.; Li, Y.-X. Transesterification of ethylene carbonate to dimethyl carbonate catalyzed by CeO_2 materials with various morphologies. *Catal. Commun.* **2018**, *106*, 6−10.
(17) Lin, B.; Liu, Y.; Heng, L.; Ni, J.; Lin, J.; Jiang, L. Effect of ceria morphology on the catalytic activity of Co/CeO_2 catalyst for ammonia synthesis. *Catal. Commun.* **2017**, *101*, 15−19.
(18) He, W.; Ran, J.; Niu, J.; Yang, G.; Ou, Z.; He, Z. Insight into the effect of facet-dependent surface and oxygen vacancies of CeO_2 for Hg removal: From theoretical and experimental studies. *J. Hazard. Mater.* **2020**, *397*, 122646.
(19) Sayle, T.X.T.; Parker, S.C.; Catlow, C.R.A. The role of oxygen vacancies on ceria surfaces in the oxidation of carbon monoxide. *Surf. Sci.* **1994**, *316*, 329−336.
(20) Stelmachowski, P.; Ciura, K.; Indyka, P.; Kotarba, A. Facile synthesis of ordered CeO_2 nanorod assemblies: Morphology and reactivity. *Mater. Chem. Phys.* **2017**, *201*, 139−146.
(21) Kim, H. J.; Jang, M. G.; Shin, D.; Han, J. W. Design of Ceria Catalysts for Low-Temperature CO Oxidation. *ChemCatChem* **2020**, *12*, 11−26.
(22) Wang, X.; Wu, J.; Wang, J.; Xiao, H.; Chen, B.; Peng, R.; Fu, M.; Chen, L.; Ye, D.; Wen, W. Methanol plasma-catalytic oxidation over CeO2 catalysts: Effect of ceria morphology and reaction mechanism. *Chem. Eng. J.* **2019**, *369*, 233−244.
(23) Umar, A.; Almas, T.; Ibrahim, A. A.; Kumar, R.; AlAssiri, M. S.; Baskoutas, S.; Akhtar, M. S. An efficient chemical sensor based on CeO_2 nanoparticles for the detection of acetylacetone chemical. *J. Electroanal. Chem.* **2020**, *864*, 114089.
(24) Tana; Zhang, M.; Li, J.; Li, H.; Li, Y.; Shen, W. Morphology-dependent redox and catalytic properties of CeO_2 nanostructures: Nanowires, nanorods and nanoparticles. *Catal. Today* **2009**, *148*, 179−183.
(25) Du, X.; Zhang, D.; Shi, L.; Gao, R.; Zhang, J. Morphology Dependence of Catalytic Properties of Ni/ CeO_2 Nanostructures for Carbon Dioxide Reforming of Methane. *J. Phys. Chem. C* **2012**, *116*, 10009−10016.
(26) Yan, L.; Yu, R.; Chen, J.; Xing, X. Template-Free Hydrothermal Synthesis of CeO_2 Nano-octahedrons and Nanorods: Investigation of the Morphology Evolution. *Cryst. Growth Des.* **2008**, *8*, 1474−1477.
(27) Zheng, X.; Li, Y.; Zhang, L.; Shen, L.; Xiao, Y.; Zhang, Y.; Au, C.; Jiang, L. Insight into the effect of morphology on catalytic performance of porous CeO_2 nanocrystals for H_2S selective oxidation. *Appl. Catal., B* **2019**, *252*, 98−110.
(28) Kang, D.; Yu, X.; Ge, M. Morphology-dependent properties and adsorption performance of CeO_2 for fluoride removal. *Chem. Eng. J.* **2017**, *330*, 36−43.
(29) Miceli, P.; Bensaid, S.; Russo, N.; Fino, D. Effect of the morphological and surface properties of CeO_2-based catalysts on the soot oxidation activity. *Chem. Eng. J.* **2015**, *278*, 190−198.
(30) Chang, H.-Y.; Chen, H.-I. Morphological evolution for CeO_2 nanoparticles synthesized by precipitation technique. *J. Cryst. Growth* **2005**, *283*, 457−468.
(31) Li, Z.; Niu, X.; Lin, Z.; Wang, N.; Shen, H.; Liu, W.; Sun, K.; Fu, Y. Q.; Wang, Z. Hydrothermally synthesized CeO_2 nanowires for H_2S sensing at room temperature. *J. Alloys Compd.* **2016**, *682*, 647−653.
(32) Mock, S. A.; Sharp, S. E.; Stoner, T. R.; Radetic, M. J.; Zell, E. T.; Wang, R. CeO_2 nanorods-supported transition metal catalysts for CO oxidation. *J. Colloid Interface Sci.* **2016**, *466*, 261−267.
(33) Ferreira, N. S.; Angélica, R. S.; Marques, V. B.; de Lima, C. C. O.; Silva, M. S. Cassava-starch-assisted sol−gel synthesis of CeO_2 nanoparticles. *Mater. Lett.* **2016**, *165*, 139−142.
(34) He, D.; Hao, H.; Chen, D.; Lu, J.; Zhong, L.; Chen, R.; Liu, F.; Wan, G.; He, S.; Luo, Y. Rapid synthesis of nano-scale CeO_2 by microwave-assisted sol−gel method and its application for CH_3SH catalytic decomposition. *J. Environ. Chem. Eng.* **2016**, *4*, 311−318.
(35) Krishnan, A.; Sreeremya, T. S.; Ghosh, S. Morphological evolution and growth of cerium oxide nanostructures by virtue of organic ligands as well as monomer concentration. *CrystEngComm* **2015**, *17*, 7094−7106.
(36) Lin, M.; Fu, Z. Y.; Tan, H. R.; Tan, J. P. Y.; Ng, S. C.; Teo, E. Hydrothermal Synthesis of CeO_2 Nanocrystals: Ostwald Ripening or Oriented Attachment? *Cryst. Growth Des.* **2012**, *12*, 3296−3303.
(37) Araújo, V. D.; Avansi, W.; de Carvalho, H. B.; Moreira, M. L.; Longo, E.; Ribeiro, C.; Bernardi, M. I. B. CeO_2 nanoparticles synthesized by a microwave-assisted hydrothermal method: evolution from nanospheres to nanorods. *CrystEngComm* **2012**, *14*, 1150−1154.
(38) Deus, R. C.; Cilense, M.; Foschini, C. R.; Ramirez, M. A.; Longo, E.; Simões, A. Z. Influence of mineralizer agents on the growth of crystalline CeO_2 nanospheres by the microwave-hydrothermal method. *J. Alloys Compd.* **2013**, *550*, 245−251.
(39) Litwinowicz, A.-A.; Takami, S.; Asahina, S.; Hao, X.; Yoko, A.; Seong, G.; Tomai, T.; Adschiri, T. Formation dynamics of mesocrystals composed of organically modified CeO_2 nanoparticles: analogy to a particle formation model. *CrystEngComm* **2019**, *21*, 3836−3843.
(40) Liu, X.; Yang, H.; Han, L.; Liu, W.; Zhang, C.; Zhang, X.; Wang, S.; Yang, Y. Mesoporous-shelled CeO_2 hollow nanospheres synthesized by a one-pot hydrothermal route and their catalytic performance. *CrystEngComm* **2013**, *15*, 7769.

https://dx.doi.org/10.1021/acs.cgd.0c00165
Cryst. Growth Des. 2020, 20, 5031−5042

(41) Shi, J.; Wang, H.; Liu, Y.; Ren, X.; Sun, H.; Lv, B. Rapid microwave-assisted hydrothermal synthesis of CeO_2 octahedra with mixed valence states and their catalytic activity for thermal decomposition of ammonium perchlorate. *Inorg. Chem. Front.* **2019**, *6*, 1735−1743.
(42) Tao, Y.; Tao, Y. X.; Su, Z. H.; Wu, H. P. Shape-Controlled CeO_2 Nanomaterials Prepared by Hydrothermal Process. *Appl. Mech. Mater.* **2013**, *331*, 513−521.
(43) Bezkrovnyi, O. S.; Lisiecki, R.; Kepinski, L. Relationship between morphology and structure of shape-controlled CeO_2 nanocrystals synthesized by microwave-assisted hydrothermal method. *Cryst. Res. Technol.* **2016**, *51*, 554−560.
(44) Corno, M.; Busco, C.; Civalleri, B.; Ugliengo, P. Periodic ab initio study of structural and vibrational features of hexagonal hydroxyapatite $Ca_{10}(PO_4)_6(OH)_2$. *Phys. Chem. Chem. Phys.* **2006**, *8*, 2464−2472.
(45) Graciani, J.; Marquez, A. M.; Plata, J. J.; Ortega, Y.; Hernandez, N. C.; Meyer, A.; Zicovich-Wilson, C. M.; Sanz, J. F. Comparative Study on the Performance of Hybrid DFT Functionals in Highly Correlated Oxides The Case of CeO_2 and Ce_2O_3. *J. Chem. Theory Comput.* **2011**, *7*, 56−65.
(46) Dovesi, R.; Erba, A.; Orlando, R.; Zicovich-Wilson, C. M.; Civalleri, B.; Maschio, L.; Rérat, M.; Casassa, S.; Baima, J.; Salustro, S.; Kirtman, B. Quantum-mechanical condensed matter simulations with CRYSTAL. *Wiley Interdiscip. Rev. Comput. Mol. Sci.* **2018**, *8*, e1360.
(47) Yuan, Q.; Duan, H. H.; Li, L. L.; Sun, L. D.; Zhang, Y. W.; Yan, C. H. Controlled synthesis and assembly of ceria-based nanomaterials. *J. Colloid Interface Sci.* **2009**, *335*, 151−167.
(48) Wu, N.-C.; Shi, E.-W.; Zheng, Y.-Q.; Li, W.-J. Effect of pH of Medium on Hydrothermal Synthesis of Nanocrystalline Cerium(IV) Oxide Powders. *J. Am. Ceram. Soc.* **2002**, *85*, 2462−2468.
(49) Zhang, Y.; Bals, S.; Van Tendeloo, G. Understanding CeO_2-Based Nanostructures through Advanced Electron Microscopy in 2D and 3D. *Part Part Syst. Charact.* **2019**, *36*, 1800287.
(50) Byzynski, G.; Melo, C.; Volanti, D. P.; Ferrer, M. M.; Gouveia, A. F.; Ribeiro, C.; Andrés, J.; Longo, E. The interplay between morphology and photocatalytic activity in ZnO and N-doped ZnO crystals. *Mater. Des.* **2017**, *120*, 363−375.
(51) Ferrer, M. M.; Gouveia, A. F.; Gracia, L.; Longo, E.; Andrés, J. A 3D platform for the morphology modulation of materials: first principles calculations on the thermodynamic stability and surface structure of metal oxides: Co_3O_4, α-Fe_2O_3, and In_2O_3. Model. *Modell. Simul. Mater. Sci. Eng.* **2016**, *24*, 025007.
(52) Omar, M. S. Models for mean bonding length, melting point and lattice thermal expansion of nanoparticle materials. *Mater. Res. Bull.* **2012**, *47*, 3518−3522.
(53) Bae, I.-T.; Ichinose, T.; Yasui, S.; Kovács, A.; Zhao, H. J.; Íñiguez, J.; Naganuma, H. Strategy to utilize transmission electron microscopy and X-ray diffraction to investigate biaxial strain effect in epitaxial $BiFeO_3$ films. *Jpn. J. Appl. Phys.* **2018**, *57*, 0902A5.
(54) Zhang, F. X.; Tracy, C. L.; Lang, M.; Ewing, R. C. Stability of fluorite-type $La_2Ce_2O_7$ under extreme conditions. *J. Alloys Compd.* **2016**, *674*, 5.
(55) Hull, S.; Norberg, S. T.; Ahmed, I.; Eriksson, S. G.; Marrocchelli, D.; Madden, P. A. Oxygen vacancy ordering within anion-deficient Ceria. *J. Solid State Chem.* **2009**, *182*, 2815−2821.
(56) Yashima, M.; Takizawa, T. Atomic Displacement Parameters of Ceria Doped with Rare-Earth Oxide $Ce_{0.8}R_{0.2}O_{1.9}$(R = La, Nd, Sm, Gd, Y, and Yb) and Correlation with Oxide-Ion Conductivity. *J. Phys. Chem. C* **2010**, *114*, 2385.
(57) Yashima, M.; Kobayashi, S.; Yasui, T. Crystal structure and the structural disorder of ceria from 40 to 1497 °C. *Solid State Ionics* **2006**, *177*, 211−215.
(58) Yashima, M.; Kobayashi, S. Positional disorder of oxygen ions in ceria at high temperatures. *Appl. Phys. Lett.* **2004**, *84*, 526−528.
(59) Kummerle, E. A.; Heger, G. The Structures of $C^+Ce_2O_31d$, Ce_7O_{12}, and $Ce_{11}O_{20}$. *J. Solid State Chem.* **1999**, *147*, 485−500.
(60) WoŁcyrz, M.; Kepinski, L. Rietveld Refinement of the Structure of CeOCl Formed in PdlCeO, Catalyst: Notes on the Existence of a Stabilized Tetragonal Phase of La,O, in La-Pd-0 System. *J. Solid State Chem.* **1992**, *99*, 409−413.
(61) Modhera, B.; Chakraborty, M.; Parikh, P. A.; Jasra, R. V. Synthesis of nano-crystalline zeolite β: Effects of crystallization parameters. *Cryst. Res. Technol.* **2009**, *44*, 379−385.
(62) Zhou, H.; Mao, Y.; Wong, S. S. Shape control and spectroscopy of crystalline $BaZrO_3$ perovskite particles. *J. Mater. Chem.* **2007**, *17*, 1707−1713.
(63) Spanier, J. E.; Robinson, R. D.; Zhang, F.; Chan, S.-W.; Herman, I. P. Size-dependent properties of CeO_2−ynanoparticles as studied by Raman scattering. *Phys. Rev. B: Condens. Matter Mater. Phys.* **2001**, *64*, 245407.
(64) Han, W.-Q.; Wu, L.; Zhu, Y. Formation and Oxidation State of CeO_{2-x} Nanotubes. *J. Am. Chem. Soc.* **2005**, *127*, 12814−12815.
(65) Palard, M.; Balencie, J.; Maguer, A.; Hochepied, J.-F. Effect of hydrothermal ripening on the photoluminescence properties of pure and doped cerium oxide nanoparticles. *Mater. Chem. Phys.* **2010**, *120*, 79−88.
(66) Campbell, C. T.; Peden, C. H. *Science* **2005**, *309*, 713−714.
(67) Nolan, M. Enhanced oxygen vacancy formation in ceria (111) and (110) surfaces doped with divalent cations. *J. Mater. Chem.* **2011**, *21*, 9160.
(68) Zhang, D.; Du, X.; Shi, L.; Gao, R. Shape-controlled synthesis and catalytic application of ceria nanomaterials. *Dalton trans.* **2012**, *41*, 14455−14475.
(69) Kubelka, P.; Munk, F. Ein Beitrag Zur Optik Der Farbanstriche. *Zeitschrift für Technische Physik* **1931**, *12*, 593.
(70) Wood, D. L.; Tauc, J. Weak Absorption Tails in Amorphous Semiconductors. *Phys. Rev. B* **1972**, *5*, 3144−3151.
(71) Zhou, G.; Yao, Y.; Zhao, X.; Liu, X.; Sun, B.; Zhou, A. Band gap energies for white nanosheets/yellow nanoislands/purple nanorods of CeO_2. *RSC Adv.* **2016**, *6*, 59370−59374.
(72) Ko, H.-H.; Yang, G.; Wang, M.-C.; Zhao, X. Isothermal crystallization kinetics and effect of crystallinity on the optical properties of nanosized CeO_2 powder. *Ceram. Int.* **2014**, *40*, 6663−6671.
(73) Ko, H.-H.; Yang, G.; Cheng, H.-Z.; Wang, M.-C.; Zhao, X. Growth and optical properties of cerium dioxide nanocrystallites prepared by coprecipitation routes. *Ceram. Int.* **2014**, *40*, 4055−4064.
(74) Phoka, S.; Laokul, P.; Swatsitang, E.; Promarak, V.; Seraphin, S.; Maensiri, S. Synthesis, structural and optical properties of CeO_2 nanoparticles synthesized by a simple polyvinyl pyrrolidone (PVP) solution route. *Mater. Chem. Phys.* **2009**, *115*, 423−428.
(75) Longo, V. M.; Cavalcante, L. S.; de Figueiredo, A. T.; Santos, L. P. S.; Longo, E.; Varela, J. A.; Sambrano, J. R.; Paskocimas, C. A.; De Vicente, F. S.; Hernandes, A. C. Highly intense violet-blue light emission at room temperature in structurally disordered $SrZrO_3$ powders. *Appl. Phys. Lett.* **2007**, *90*, 091906.
(76) Kim, I.-D.; Rothschild, A.; Tuller, H. L. Advances and new directions in gas-sensing devices. *Acta Mater.* **2013**, *61*, 974−1000.
(77) Deus, R. C.; Amoresi, R. A. C.; Desimone, P. M.; Schipani, F.; Rocha, L. S. R.; Ponce, M. A.; Simoes, A. Z.; Longo, E. Electrical behavior of cerium dioxide films exposed to different gases atmospheres. *Ceram. Int.* **2016**, *42*, 15023−15029.
(78) Ortega, P. P.; Rocha, L. S. R.; Cortés, J. A.; Ramirez, M. A.; Buono, C.; Ponce, M. A.; Simões, A. Z. Towards carbon monoxide sensors based on europium doped cerium dioxide. *Appl. Surf. Sci.* **2019**, *464*, 692−699.
(79) Amorim, C. A.; Bernardo, E. P.; Leite, E. R.; Chiquito, A. J. Effect of inhomogeneous Schottky barrier height of SnO_2 nanowires device. *Semicond. Sci. Technol.* **2018**, *33*, 055003.
(80) Teixeira, M. M.; de Oliveira, R. C.; Oliveira, M. C.; Pontes Ribeiro, R. A.; de Lazaro, S. R.; Li, M. S.; Chiquito, A. J.; Gracia, L.; Andres, J.; Longo, E. Computational Chemistry Meets Experiments for Explaining the Geometry, Electronic Structure, and Optical Properties of $Ca_{10}V_6O_{25}$. *Inorg. Chem.* **2018**, *57*, 15489−15499.

https://dx.doi.org/10.1021/acs.cgd.0c00165
Cryst. Growth Des. 2020, 20, 5031−5042